Article

Not peer-reviewed version

Latent Bacterial Cells Residing Inside Macrophages Can Be Spotted With pH-sensitive Fluorescent FRET Probe in Polymeric Micellar Formulation

Igor D. Zlotnikov , Alexander A. Ezhov , Natalya G. Belogurova , Elena V. Kudryashova *

Posted Date: 6 August 2024

doi: 10.20944/preprints202408.0285.v1

Keywords: theranostics; FRET marker; pH sensitivity; bacterial infections; visualization; macrophage

Article

Latent Bacterial Cells Residing Inside Macrophages Can Be Spotted with pH-Sensitive Fluorescent FRET Probe in Polymeric Micellar Formulation

Igor D. Zlotnikov [1], Alexander A. Ezhov [2], Natalya G. Belogurova [1] and Elena V. Kudryashova [1,*]

[1] Faculty of Chemistry, Lomonosov Moscow State University, Leninskie Gory, 1/3, 119991 Moscow, Russia; zlotnikovid@my.msu.ru, nbelog@mail.ru (N.G.B.)

[2] Faculty of Physics, Lomonosov Moscow State University, Leninskie Gory, 1/2, 119991 Moscow, Russia; alexander-ezhov@yandex.ru (A.A.E.)

* Correspondence: helena_koudriachova@hotmail.com (E.V.K.)

Abstract: As shown previously, Rhodamine 6G (R6G) and 4-nitro-2,1,3-benzoxadiazole (NBD) linked through a spacer molecule spermidine (spd), R6G-spd-NBD, produce a fluorescent probe with pH-sensitive FRET effect, that can be useful in a variety of diagnostic applications. Specifically, cancer cells can be spotted due to a local decrease in pH (Warburg effect). Here we extend this approach to infectious diseases – namely, leishmaniasis, brucellosis, and tuberculosis, are difficult to treat largely because of their localization inside macrophages. R6G-spd-NBD offers an opportunity to detect such bacteria and potentially deliver therapeutic target to treat them. The micellar form of the R6G-spd-NBD probe (chitosan or heparin grafted with lipoic acid residues, Chit-LA and Hep-LA, respectively) was obtained to improve the pH sensitivity in the desired range (5.5–7.5) and enable the selective targeting of bacterial cells, thus improving CLSM imaging. According to AFM (atomic force microscopy) data, the micelles containing NBD-spd-R6G have a compact and highly spherical shape, with a diameter ranging from 70 to 110 nm. The micellar form of the R6G-spd-NBD further improves absorption and penetration into bacteria, including those located inside macrophages. Due to negative charge of the surface, bacteria absorb positively charged R6G-spd-NBD, and even more so in the micellar form, when chitosan derivatives are used to form the polymeric micelle. Additionally, macrophages' lysosomes can be easily distinguished due to their acidic pH. Confocal laser scanning microscopy was used to visualize samples of macrophages cells containing absorbed bacteria. The micellar formulation showed a significant selectivity to model *E. coli* vs *Lactobacillus* bacterial cells, and R6G-spd-NBD, being a mild bactericide, clears over 50% *E.coli* in conditions where *Lactobacillus* remains almost unaffected. Taken together, our data indicates that R6G-spd-NBD, as well as similar compounds, can have value not only for diagnostic, but also for theranostic applications.

Keywords: theranostics; FRET marker; pH sensitivity; bacterial infections; visualization; macrophage

1. Introduction

Theranostics is a modern approach to the development of pharmaceutical formulations that serve as both early diagnostic tools and improved therapeutic agents [1–7]. This approach is particularly relevant for the treatment of severe diseases including intracellular infections, such as tuberculosis [8–11], chlamydia [12–14], brucellosis [15–19], leishmaniasis [20–22], which are difficult to treat due to intracellular localization within macrophages.

On the other hand, cancers represent a significant challenge in terms of treatment, requiring innovative and effective strategies. Theranostics and nanomedicine offer several advantages

 doi:10.20944/preprints202408.0285.v1

including improved drug distribution and accumulation, the ability to image pathogenic cells, areas of inflammation [28–30] where the nanoparticles that can accumulate in pathogenic cells and fight it.

Nanoparticles have several undeniable advantages in terms of its therapeutic effectiveness: 1) a specific size (50–200 nm) that allows them to remain in the bloodstream and only penetrate into pathogenic cells (bacteria, parasite microorganisms, or tumor) due to the specificity of its biomembranes [31]; 2) the enhanced permeability and retention (EPR) effect that promotes the accumulation of nanoparticles in the area of inflammation or in tumors microenvironment [24,32,33]; 3) chemical modifications (e.g., biocompatible polymers such as chitosan or heparin with lipoic acid residues that stimulate sensitivity to the tumor microenvironment), lead to the increased targeting, safety, and reduce systemic toxicity [34]; 4) the possibility of creating a combination for a super-effective action of nanoparticles due to synergy of the drug action [35]; 5) strengthening of the main component due to adjuvants to cytostatics or antibiotics, as we have recently shown in the works [36,37].

The targeted approach using theranostic techniques can be employed to deliver a variety of therapeutic agents, including nucleic acids, chemotherapeutics, and hyperthermic agents, among others, for subsequent applications such as photothermal ablation, photodynamic and radiation therapy [5].

There are various techniques of this approach:

1. Imaging techniques:
   - Positron emission tomography (PET)
   - Computer tomography (CT) and ^{18}F-FDG PET/CT
   - Single-photon emission computed tomography (SPECT)
   - Magnetic resonance imaging (MRI)
2. Therapeutic approaches:
   - Targeted drug delivery systems
   - Gene therapy
   - Immunotherapy
   - Nanomedicine
3. Ablation:
   - Radio frequency ablation
   - Microwave ablation
   - Cryoablation
   - Chemo-embolization
   - Selective internal radiation therapy
   - Dose painting

The application of the theranostic approach has significant potential in the elucidating the molecular and cellular mechanisms that regulate tissue response to inflammation, as well as influencing this process. The key mechanism responsible for maintaining tissue integrity and initiating tissue response to injury is the complex activity of tissue macrophages, which remove dying cells and bacteria, as well as produce a wide range of biologically active substances essential for tissue function. In barrier tissues, macrophages are present, which can be divided into several functional types. Macrophages that are classically activated (M1) protect the body against microorganisms by triggering an inflammatory response through the secretion of pro-inflammatory cytokines [38–44]. On the other hand, alternatively activated (M2) macrophages help to regulate the response to injury and inflammation by producing anti-inflammatory cytokines [45–50]. In cases of chronic or persistent inflammation, macrophages may be exposed to permonent activation signals resulting the pathological tissue changes, such as fibrosis and chronic inflammation. It has been suggested that an increased expression of the M2 macrophage phenotype is linked to fibrous tissue remodeling in internal organs such as the heart and lungs.

This highlights the importance of understanding the role of macrophages in regulating inflammation and developing strategies to treat chronic inflammation in serious infectious diseases.

 doi:10.20944/preprints202408.0285.v1

Intramacrophage infections may be "dormant" or latent, making them difficult to treat [51–53]. Therefore, exploring new approaches, such as theranostic techniques, is crucial in that cases.

In this paper, we propose the use of targeted drug delivery systems to simultaneously diagnose pathogenic bacterial infections, including latent forms within macrophages, and treat these pathogens using the same product (a fluorescent diagnostic agent and an antibiotic combined in a single formulation). The example of a disease that requires a radically new approach, such as the use of theranostics, is intramacrofagal severe brucellosis infection.

Brucellosis is an infectious disease, characterized by a variety of pathological changes in multiple organs and a propensity for chronicity [54–58]. The causative agents of brucellosis are bacteria belonging to the genus *Brucella*. Brucellosis is a highly virulent disease that exhibits severe symptoms, and its intracellular nature poses significant challenges for diagnosis and treatment. Even the most advanced diagnostic techniques may struggle to detect and manage this condition effectively. Currently, eight independent species are recognized, six of which can cause serious disease in humans.

This approach has the potential to improve patient outcomes by providing a more efficient and targeted treatment, as well as allowing for the monitoring of disease progression and the adjustment of treatment plans. Furthermore, this method could lead to the development of individualized treatment strategies, opening up new possibilities for personalized and highly effective medical care. Recently, we developed a pH-sensitive fluorescent marker that specifically stains cancer cells compared to normal cells due to differences in their microenvironment (Warburg effect) [59]. The pH probe is a conjugated form of rhodamine 6G (R6G) and 4-nitro-2,1,3-benzoxadiazole (NBD), linked via a spacer molecule, spermidine (spd), which, due to protonation, ensures the pH sensitivity of the fluorescent conjugate, and also FRET is realized between the NBD donor and the R6G acceptor when the probe enters the target cells. The micellar form (chitosan-lipoic acid polymeric micelles, Chit-LA) of the pH probe exhibited high sensitivity to changes in acidity of the surrounding medium [31,35]. Based on the results obtained from this study, we propose a formulation based on R6G-spd-NBD for selective staining of bacterial cells in macrophages.

2. Results and Discussion

2.1. Work Design

The primary objective of this study is to develop a theranostic agent R6G-spd-NBD, with regard to its antibacterial activity and its potential for diagnosing pathogens. The micellar form of the R6G-spd-NBD probe, which is chitosan or heparin that has been grafted with lipoic acid residues (Chit-LA and Hep-LA, respectively), has been designed to improve sensitivity to changes in the intracellular environment and serves as a marker to distinguish between model bacterial cells of *Escherichia coli* (*E. coli*) and *Lactobacillus* species.

The following key objectives are:

1. Synthesis of NBD-spd-R6G and creation of a micellar formulation, as well as spectral characterization of the drug.

2. Investigation of the fluorescent properties of NBD-spd-R6G in both free and micellar forms, in buffer solution, and after exposure in vitro to *E. coli* or *Lactobacillus* bacterial cells.

3. Determination of the antibacterial effects of NBD-spd-R6G and R6G and the search for a correlation with permeability to bacterial cells.

4. The visualization of the penetration of NBD-spd-R6G into bacterial cells using confocal fluorescence microscopy.

5. Study of model latent bacterial infections localized within macrophages, with a focus on diagnosis and treatment.

6. Discussion of the potential diagnostic and medicinal applications of the formulated products, as well as identification of potential uses.

 doi:10.20944/preprints202408.0285.v1

2.2. Synthesis, Characterization, and Preparation of the Micellar Formulation of NBD-spd-R6G

Figure 1a illustrates the conjugate structure of rhodamine 6G (R6G) and 4-nitro-2,1,3-benzoxadiazole (NBD), which are linked via a spacer molecule, spermidine (spd), as well as FTIR spectra of the NBD-spd-R6G conjugate in comparison to R6G alone. The synthesis of NBD-spd-R6G was carried out in four stages (Figure S1): 1) protection of spd NH_2 group with 4-hydroxybenzaldehyde HO-C_6H_4-CHO by the formation of a Schiff base HO-C_6H_4-HC=N-spd that was confirmed by the appearance of FTIR peak at 1645 cm^{-1} ν(C=N) (Figure S2); 2) HO-C_6H_4-HC=N-spd reacted with NBD-Cl via the S_NAr reaction; 3) deprotection of spermidine NH_2 group with the formation NBD-spd, which is reflected in an intensity increase of FTIR ν(N–H) peaks (3600–3300 cm^{-1}, 3100–2750 cm^{-1}) and disappearance of the ν(C=C) peaks of the 4-hydroxybenzaldehyde (1560–1615 cm^{-1}) (Figure S2); 4) The final stage is the crosslinking of NBD-spd with rhodamine 6G (R6G) via the formation of an amide bond from an ester and an amine that was confirmed both by the disappearance of FTIR ν(ester C=O) peak in free R6G (1730-1710 cm^{-1}) and the appearance of the peaks of FTIR ν(amide C=O) 1690–1650 cm^{-1}, δ(amide N–H) 1580 cm^{-1} (Figure 1a). FIIR spectroscopy confirms the formation of the chemical conjugate NBD-spd-R6G, additional validation of the drug carried out using the complementary NMR spectroscopy method.

The following important signals are observed in the NMR proton spectrum of a substance NBD-spd (Figure S3): aromatic 7.8, 7.5 ppm (–CH=C(NO_2)–) and 7.1, 6.9 ppm (–CH=C(NR)–) and signals referenced to the spermidine spacer in range of 1.1–3.0 ppm, which are in a good agreement with the literature data for NBD and similar compounds [60–63]. Figure 1bc shows the ^1H and ^{13}C NMR spectra of NBD-spd-R6G. In the ^1H NMR spectrum of NBD-spd-R6G, signals are observed in the region of 6-8 ppm, which corresponds to protons in the aromatic system of R6G. In the ^{13}C NMR spectrum, signals in the range 118-153 ppm are referenced to C-atoms in the aromatic systems of R6G or NBD. ^{13}C NMR signals at 14-21 ppm correspond to C-atoms in CH_3 and CH_2 groups of spd spacer. NMR peaks at 169 and 173 ppm correspond to C-atom in amide bond between R6G and NBD-spd (Figure 1c). Therefore, NMR spectroscopy has confirmed the formation of NBD-spd-R6G.

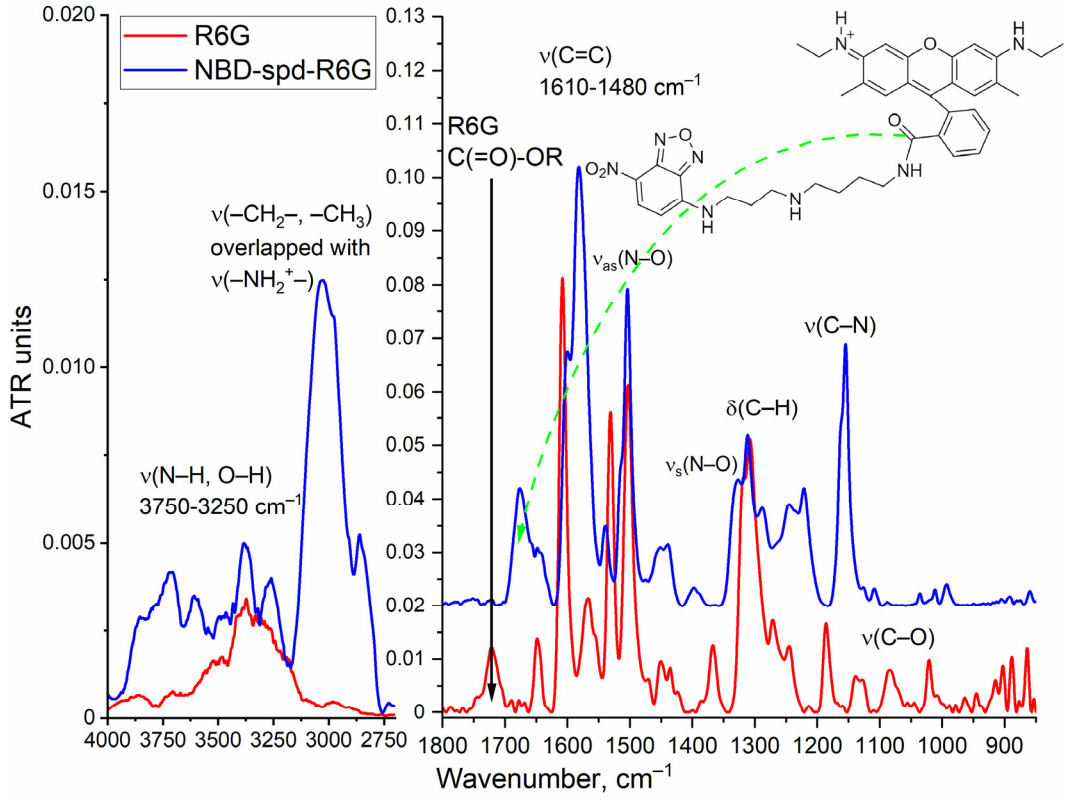

(a)

 doi:10.20944/preprints202408.0285.v1

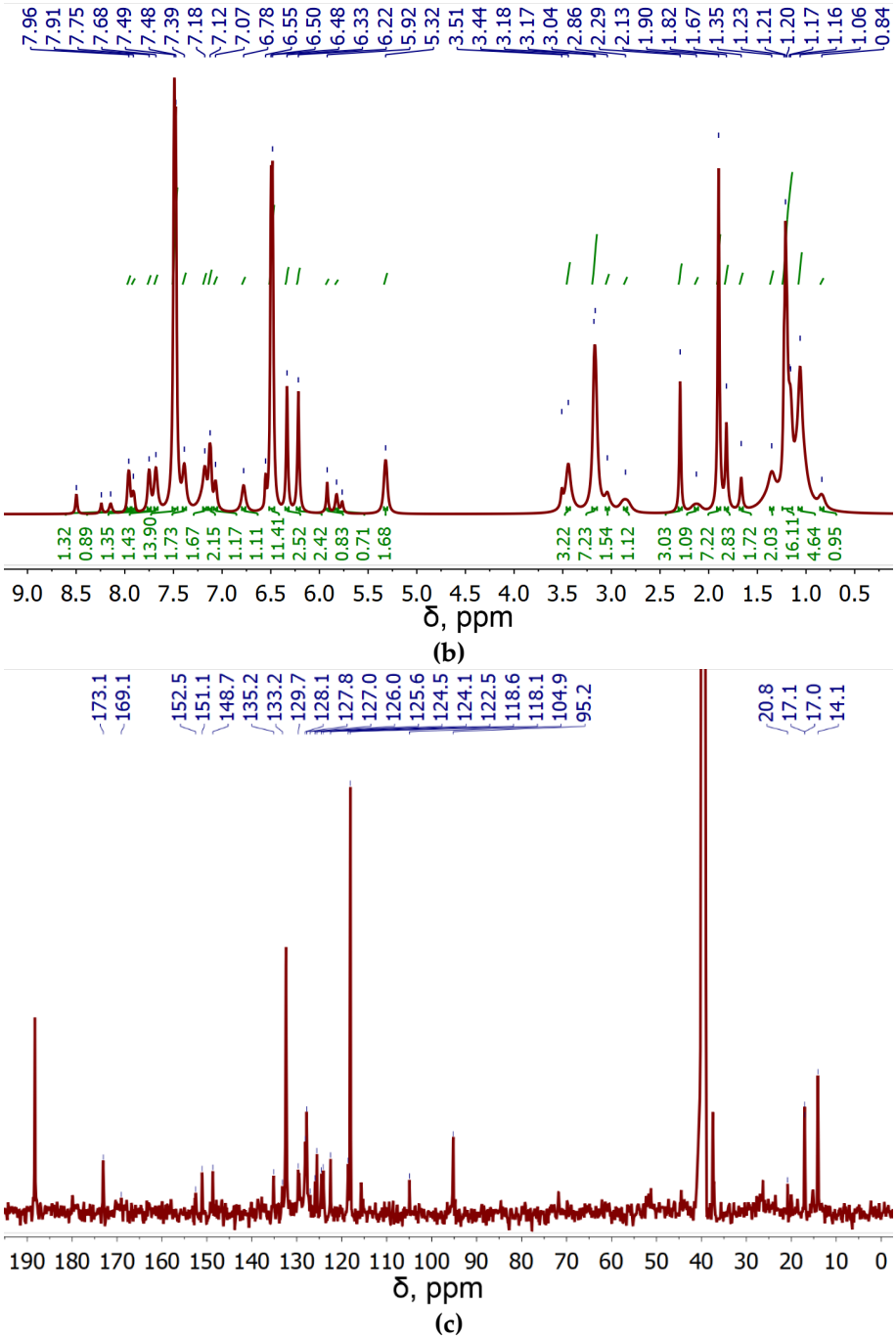

Figure 1. (a) FTIR spectra and structure of theranostic agent NBD-spd-R6G. PBS (0.01M, pH = 7.4). **(b)** ^{1}H NMR spectra of NBD-spd-R6G. (**c**) ^{13}C NMR spectra of NBD-spd-R6G. T = 22 °C. DMSO-d$_6$. Working frequencies: 500.13 MHz (^{1}H) and 125.76 MHz (^{13}C).

Figure 2a illustrates a schematic representation of the micellar formulation with the theranostic agent NBD-spd-R6G. We used amphiphilic polymers, chitosan-lipoic acid (Chit-LA), as they spontaneously form micelles that, on the one hand, facilitate the solubilization and loading of the fluorophore into the hydrophobic core of the micelle, and on the other hand, allow for the selective release of the agent when exposed to a triggering stimulus (pH, temperature, glutathione GSH, chemical stimuli). This would significantly enhance the diagnostic and therapeutic capabilities of NBD-spd-R6G. We used chitosan-lipoic acid micelles (Chit-LA) with a positive charge (ζ = +8 mV) compared to heparin-lipoic acid micelles (Hep-LA) with a negative charge (ζ = –12 mV).

Preprints.org (www.preprints.org) | NOT PEER-REVIEWED | Posted: 6 August 2024 doi:10.20944/preprints202408.0285.v1

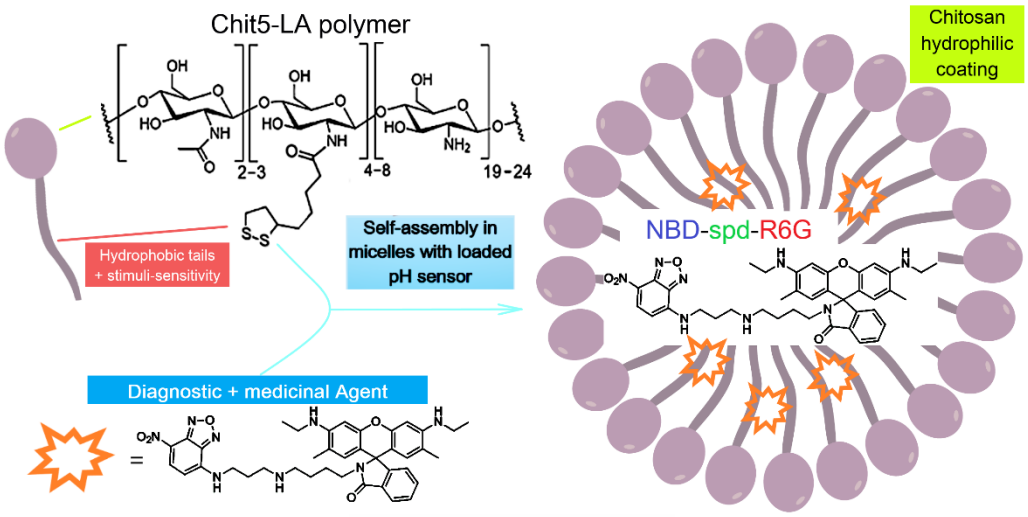

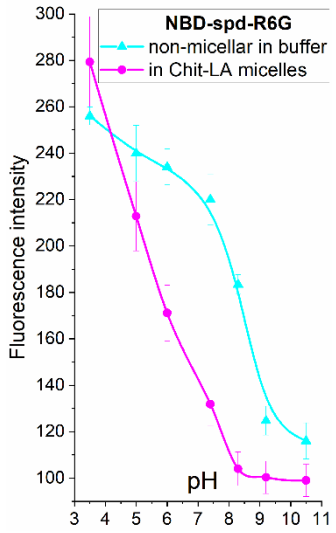

(a)

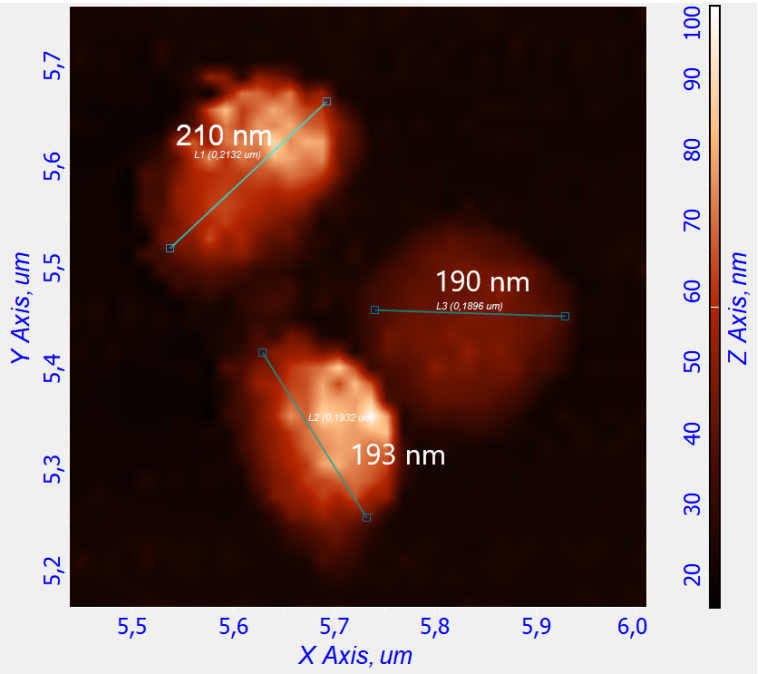

(b)

Preprints.org (www.preprints.org) | NOT PEER-REVIEWED | Posted: 6 August 2024 doi:10.20944/preprints202408.0285.v1

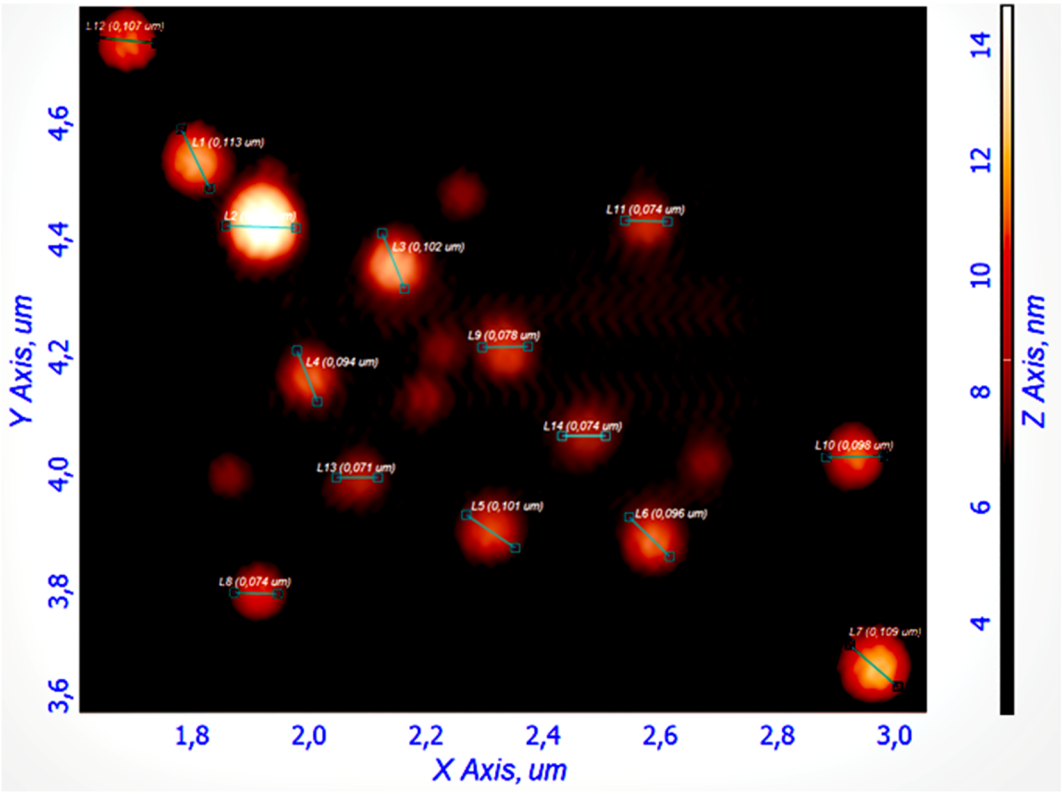

(c)

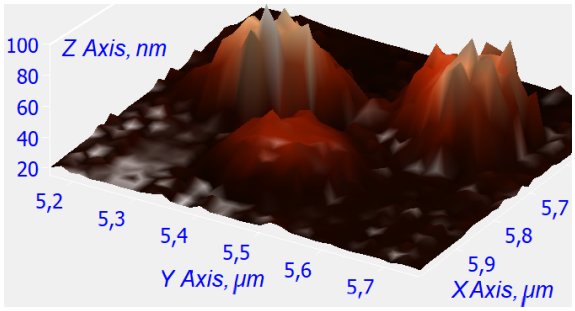

(d)

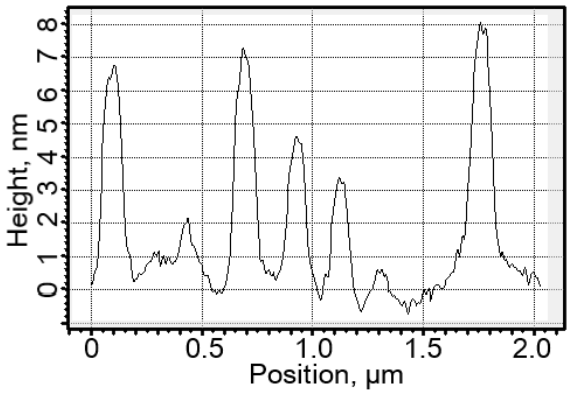

(e)

Figure 2. (a) A schematic cartoon representation of the micellar theranostic agent NBD-spd-R6G with pH-sensitivity function (shown in the right insert). (**b**) Atomic force microscopy images of non-loaded Chit5-LA polymeric micelles in 2D view. (**c**) Atomic force microscopy images of Chit5-LA micelles loaded with R6G-spd-NBD (10 mass.%). (**d**) Atomic force microscopy images of non-loaded Chit5-LA polymeric micelles in 3D view. **(e)** The corresponding height section of (c) through the main diagonal from top to bottom.

The structure of the micelles is investigated using atomic force microscopy (AFM), as shown in Figures 2b–e. Empty micelles have a distorted-spherical shape and are approximately 190–210 nm in size. In this instance, the micelles containing NBD-spd-R6G become compact (the aromatic molecules of the drug acting as a type of seed/primer) and take on a highly spherical shape with a diameter ranging from 70 to 110 nm.

 doi:10.20944/preprints202408.0285.v1

2.3. Fluorescent Properties of the Micellar Theranostic (Diagnostic+Treatment) Agent NBD-spd-R6G in Interaction with Bacterial Cells

2.3.1. Fluorescence Spectra

Figure 3 shows the fluorescent spectra of the micellar formulation of the theranostic agent NBD-spd-R6G compared with the control sample R6G in buffer solution (a-b), when exposed to *E. coli* (c-d), and to *Lactobacillus* bacteria (e-f). The spectra for mixtures (without incubation) and for samples after 2 hours of incubation with cells at 37 °C are analyzed. We studied Chit-LA positive charged micelles in comparison with Hep-LA with a negative charge.

In the buffer solution, the fluorescence intensity of NBD-spd-R6G in the non-micellar form and in micellar Chit-LA is 60-70% higher than for R6G samples, while in the micellar form of Hep-LA, the fluorescence intensity is almost the same for NBD-spd-R6G and R6G (Figure 3ab). Thus, positively charged micelles augment the fluorescence intensity of probes, either slightly or not at all, whereas negatively charged micelles diminish it. Specifically, for R6G-spd-NBD, the fluorescence intensity amounts to approximately 1,680 units in its non-micellar state, 1,600 in the presence of chitosan micelles, and 1,050 in the case of heparin-based micelles.

When exposed to *E. coli* bacterial cells, an increase in the fluorescence intensity of both NBD-spd-R6G and R6G is observed by about 2 times, while in the case of *Lactobacilli*, ignition is only 40-50% (for both fluorophores), i.e. fluorophores are sensitive specifically to model pathogenic bacteria *E. coli* vs non-pathogenic *lactobacilli*. When the fluorophore binds to bacterial cells, a shift to the short-wavelength region of the maximum fluorescence emission is observed (Figure 3cd).

NBD-spd-R6G, in its micellar Chit-LA formulation, exhibits the highest fluorescence intensity associated with *E. coli* cells, making it наиболее suitable for use in the selective detection of pathogenic bacteria. Simultaneously, the sensitivity of the NBD-spd-R6G conjugate in its micellar Chit-LA formulation exhibits a higher value compared to that of the formulation containing R6G, with an intensity of fluorescence measured at 3010 versus 2770 units, respectively.

To explain the observed effect, we turn to the pH dependence of NBD-spd-R6G in micelles Chit-LA, which demonstrated the pH sensitivity of the NBD-spd-R6G probe (Figure 2a), also studied in detail in our recent work [59]. The data (Figure 2a) indicate that the transition of the probe from the micellar environment into different bacterial cells would affect its fluorescence intensity.

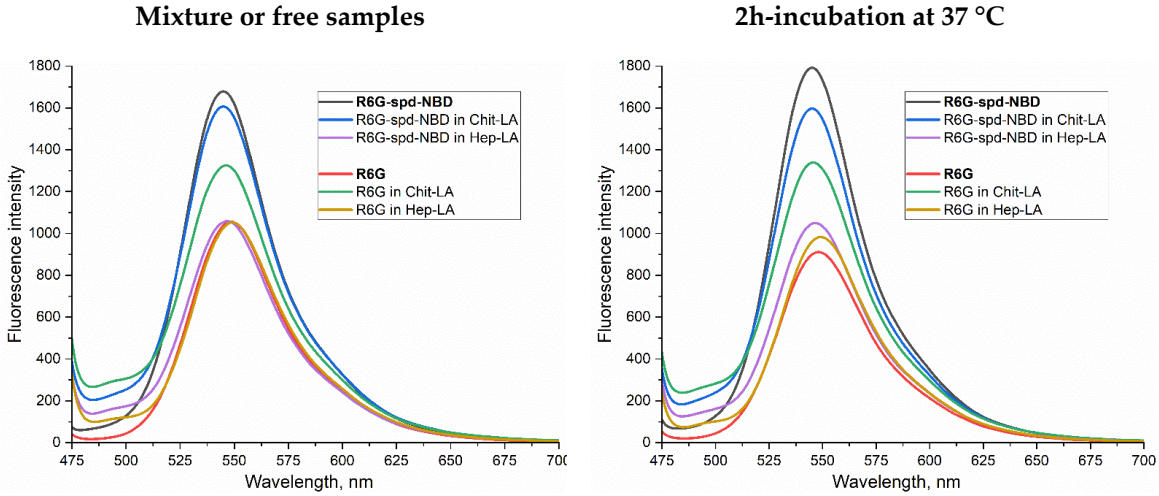

(a) **(b)**

 doi:10.20944/preprints202408.0285.v1

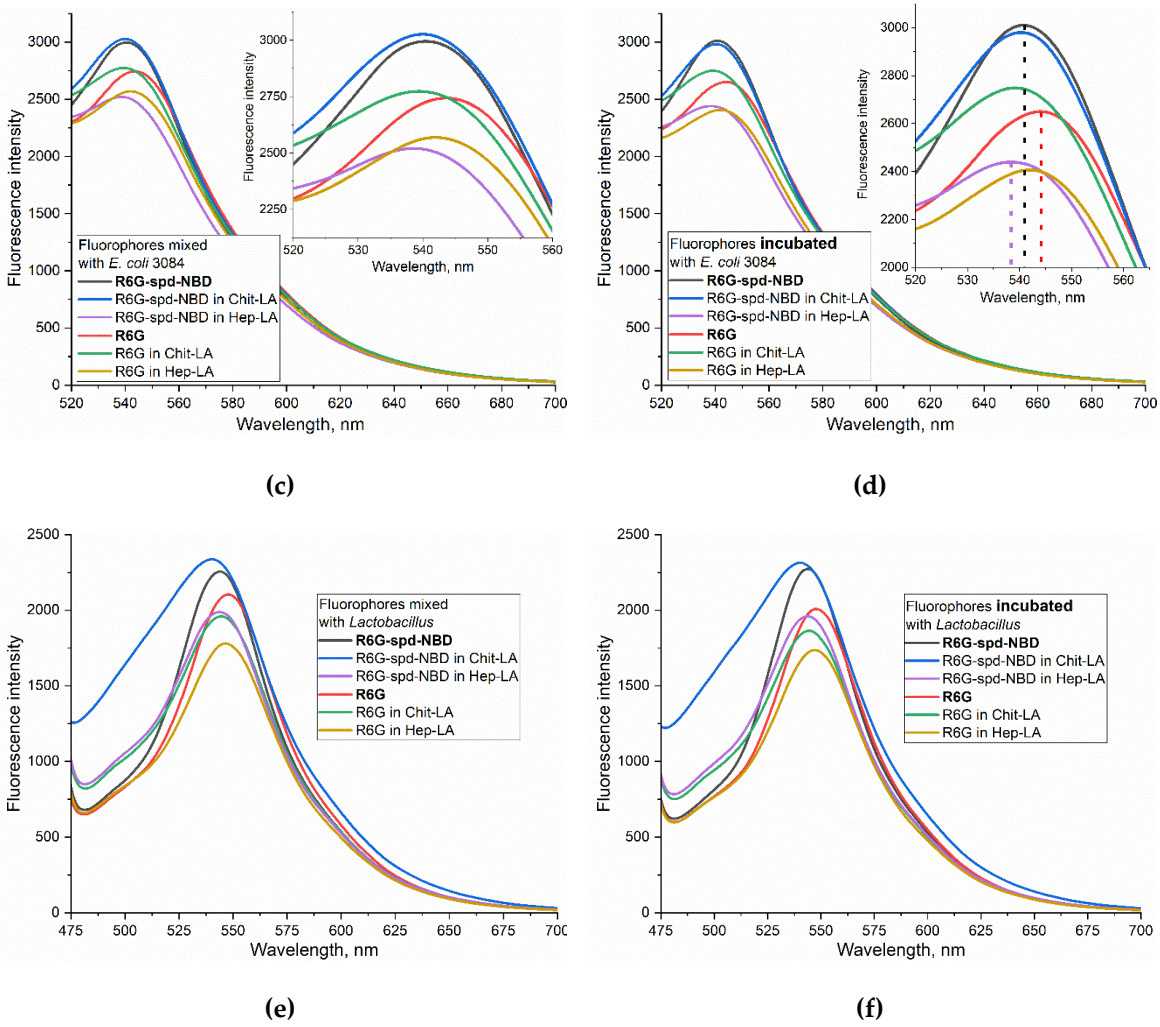

Figure 3. Fluorescence emission spectra of R6G (1 μM) and the pH sensor R6G-spd-NBD (1 μM): 1) in PBS buffer **(a)** prior to and **(b)** following a 2-hour incubation at 37 °C; 2) mixed with an *E. coli* bacterial suspension (10^7 CFU/mL) in PBS **(c)** prior to and **(d)** following a 2-hour incubation at the same temperature; 3) mixed with a *lactobacillus* suspension (10^7 CFU/mL) in PBS **(e)** prior to and **(f)** following the same incubation period at 37 °C. λ_{exci} = 460 nm. PBS (0.01M, pH = 7.4). T = 37 °C.

2.3.2. The FRET Process in the Context of the Interaction between R6G-spd-NBD and Bacterial Cells

Besides pH sensitivity the theranostic the conjugate also provides the phenomenon of FRET. FRET occurs when two fluorophores are within a distance of 1-10 nm of each other and the overlapping emission and excitation spectra of two fluorophores. In the case of NBD and R6G pair, NBD has a maximum excitation peak at 488 nm, with a maximum emission at 545 nm, while R6G exhibits a maximum excitation wavelength of 525 nm, a maximum emission wavelength of 550 nm. When NBD-spd conjugated with R6G to form R6G-spd-NBD, fluorescence excitation shifts towards shorter wavelengths compared to free R6G, resulting in a broader emission peak due to the FRET effect. The efficiency of this process is approximately 38%, assuming a fixed interplanar distance between R6G and NBD of 8.7 angstroms [59]. As result NBD-spd serves as an efficient fluorophore donor for R6G in these conjugates.

An important parameter that characterizes the interaction between bacterial cells and fluorophores or micelles is the fluorescence intensity, and which is more specific, its change. This parameter is measured as the derivative of the corresponding kinetic curves: Figure 4a shows the slope values for kinetic curves that characterize the interaction of NBD-spd-R6G or R6G samples in free form compared to the micellar formulations, with two types of cells *E. coli* and *Lactobacilli*.

 doi:10.20944/preprints202408.0285.v1

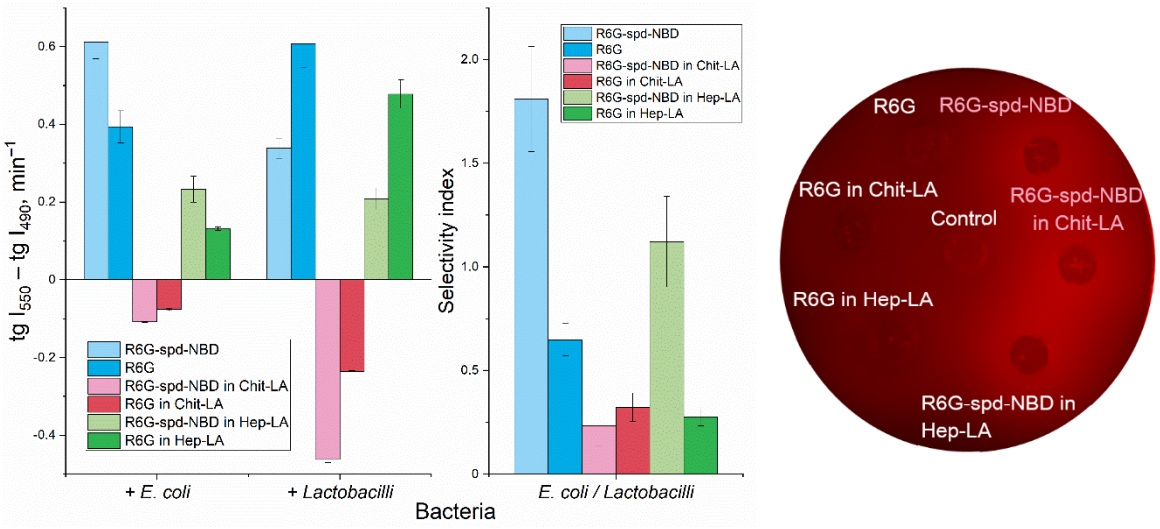

(a) **(b)**

Figure 4. (a) Kinetic parameters for the 1-hour interaction between R6G or R6G-spd-NBD pH sensor with *E. coli* and *lactobacillus* suspensions (10^7 CFU/mL): the slopes of the fluorescence emission intensity curves at 490 nm (NBD > R6G) and 550 nm (R6G > NBD). The ratio of tangents of kinetic lines at 490 nm and 550 nm for *E. coli* and *lactobacillus*. λ_{exci} = 460 nm. PBS (0.01M, pH = 7.4). T = 37 °C. **(b)** Fluorescent image of a Petri dish with *E. coli* cells (10^7 CFU / 0.5 mL placed onto 20 mL of agarized medium) when exposed to R6G or R6G-spd-NBD in non-micellar and micellar form for 12 h at 37 °C. The fluorophores are placed in wells with a diameter of 9 mm. The concentration of fluorophores is 0.1 mg/mL, the concentration of amphiphilic polymers is 0.5 mg/mL. $\lambda_{exci,\ max}$ = 480 nm. λ_{emi} = 515-570 nm.

When measuring the fluorescence of the NBD-SPD-R6G conjugate, the fluorescence signals at 490 and 550 nm correspond mainly to NBD and Rhodamine respectively (NBD > R6G and NBD < R6G). Therefore, we can independently monitor the change in the signal from NBD and rhodamine (as part of the conjugate) as the fluorophore adsorbs and penetrate into the cells. To characterize the efficiency of the interaction of fluorophores with cells we have obtained kinetic curves for the changes in fluorescence of NBD and Rhodamine and determined the slope coefficients of the kinetic curve tg(I_{550}) and tg(I_{490}). It is analytically significant the difference tg(I_{550}) – tg(I_{490}), which characterize simultaneously the quenching of the NBD donor and excitation of the R6G acceptor. So that a quantitative measure of FRET efficiency is realized.

Apparently, the interaction of NBD-spd-R6G, in both its free and micellar form, is characterized by positive derivatives (tangents), which corresponds to the ignition of R6G fluorescence upon conjugate penetration into cells (Figure 4).

In order to elucidate the mechanisms underlying the observed alteration in fluorescence upon interaction between NBD-spd-R6G fluorescent probes with cells, a series of experiments were conducted using Petri dishes containing *E. coli* bacteria. The fluorescence intensity was visualized after the probes penetrated the cells (Figure 4b).

The results revealed a significant increase in fluorescence intensity upon penetration for the conjugated probe, whereas the fluorescence for the unconjugated R6G probe remained practically unchanged. This finding suggests that the mechanism responsible for the observed effect is primarily due to FRET, which can be visualized through the fluorescent channel within the Petri dish containing the *E. coli* cultures (Figure 4b).

2.3.4. pH Sensitivity R6G-spd-NBD in the Context of its interaction with Bacterial Cells

Only in the case of chitosan micelles the negative values of the tg are observed for both fluorophores. Here, we observe two phenomena: 1) the ignition of fluorophores as it enters bacterial cells and 2) the transition of the probe from an alkaline (chitosan cation) to an acidic

 doi:10.20944/preprints202408.0285.v1

microenvironment on the cell surface due to pH sensitivity of the fluorophore (Figure 2a). Nonetheless, as a consequence, the concentration of rhodamine and its conjugate diminishes, which implies that in this case the pH sensitivity factor is of prevailing, while FRET playing a secondary role.

The analytically important parameter is the selectivity index: the ratio between the $tg(I_{550})$ - $tg(I_{490})$ values for *E. coli* and *lactobacilli*, as shown in Figure 4a on the right panel. If the selectivity index, deviates from 1 to a greater or lesser extent, it indicates the capacity for discriminating between *E. coli* and *lactobacilli* using these formulations with varying degrees of selectivity.

2.4 Antibacterial Effect of Theranostic Formulations and Its Correlation with Permeability

In order to elucidate the correlation between the cell permeability and the antibacterial efficacy, we embarked on a series of experiments. The ability of fluorophores to penetrate bacterial cells we determined by measuring the fluorescence intensity of the solution before and after exposure to cells (Table 1). For R6G, the highest penetration is observed for non-micellar form in *E. coli* cells (the ratio of extracellular to intracellular concentration (C_{in}/C_{out}) is 3.2), while the lowest penetration occurs for R6G in chitosan micelles form in *Lactobacilli* cells with a C_{in}/C_{out} ratio of 1.4. In the latter case, there is a selective effect against *E. coli* compared to *Lactobacilli.*

In the chitosan micelles R6G exhibits a remarkable enhancement in antibacterial activity, surpassing up to 20% in terms of cellular viability against model pathogenic bacterial strains (*E. coli*), as compared to non-pathogenic ones (*Lactobacilli*) (see Table 1). This finding is promising, but it still remains insufficient for its potential application in the therapy.

The conjugate R6G-spd-NBD has demonstrated remarkable selectivity, targeted penetrating into the bacterial cells of *E. coli* versus *Lactobacilli*, with a difference in penetration of more than two times, resulting in up to 40% enhancement in the effectivity (in terms of cell viability) against pathogenic bacteria compared to normal ones (see Table 1).

This effect is achieved through a more precise targeting of the R6G-spd-NBD conjugate compared to free rhodamine, as well as by employing micellar forms that selectively bind to cells, enhancing drug availability. Simultaneously, the micelles themselves do not adversely affect cell viability.

These findings allow us to propose the use of micellar formulations of R6G-spd-NBD as a potential theranostic agent (for the diagnosis and treatment of bacterial infections).

Table 1. Antibacterial effect and cellular permeability of theranostic formulations on E. coli and Lactobacillus cells after 8 hours of incubation. LB medium at pH 7.2, 37 °C, cell concentration 10^{-7} CFU/mL, fluorophore concentration 0.05 mg/mL, amphiphilic polymer concentration 0.25 mg/mL. C_{in} – intracellular concentration of fluorophore, C – extracellular concentration of fluorophore.

Sample*	**Cell viability, %**		**C_{in}/C_{out}**	
	E. coli	*Lactobacilli*	*E. coli*	*Lactobacilli*
R6G	84±5	87±2	3.2±0.3	2.2±0.1
R6G in Chit-LA micelles	67±4	85±2	2.3±0.1	1.4±0.1
R6G in Hep-LA micelles	88±7	81±4	2.5±0.2	1.7±0.2
R6G-spd-NBD	70±3	92±1	2.1±0.2	1.4±0.1
R6G-spd-NBD in Chit-LA micelles	45±2	89±4	3.6±0.4	1.7±0.3
R6G-spd-NBD in Hep-LA micelles	62±6	93±3	2.8±0.2	1.3±0.1
Chit-LA micelles	97±1	>99	Polymers mostly adsorbed onto cell surface	
Hep-LA micelles	>99	>99		

*The concentration of Rhodamine was taken near to a semi-inhibitory level, just above the midpoint of the range, in order to allow for the enhancement of antibacterial activity through the use of micellar formulations and conjugation.

 doi:10.20944/preprints202408.0285.v1

2.5. Confocal Laser Scanning Microscopy (CLSM) for Visualization of Bacterial Cell Staining Using a Theranostic Preparation

Figure 5 shows Confocal laser scanning microscopy images of *E. coli* cells and *Lactobacilli* cells, labeled with NBD-spd, R6G or R6G-spd-NBD (1 μg/mL for all markers) in free form or loaded into Chit-LA polymeric micelles.

In the case of *E. coli* and free fluorophores stain cells (all samples), however, the highest cell/background selectivity is achieved for R6G-spd-NBD. In the case of *E. coli* and micellar fluorophores, an increase in selectivity is observed for all fluorophores in the cell/background ratio, while the R6G-spd-NBD formulation remains the leader.

In the case of *Lactobacilli*, free fluorophores stain cells (but about 20-30% weaker in terms of fluorescence intensity than for *E. coli*), however, the highest cell/background selectivity is achieved for R6G. In the case of *Lactobacilli* and micellar fluorophores, an increase in the selectivity of R6G-spd-NBD staining in the aspect of cells/background is observed, while NBD-spd and R6G practically do not stain *lactobacilli* and can be used to differentiation *E. coli* against *lactobacilli*. Conversely, R6G-spd-NBD in the composition of chitosan micelles stain *lactobacilli* cells more than 60% more intensively. Thus, we have selected a whole set of diagnostic tools for the visualization of bacteria.

At the same time, R6G-spd-NBD, in its micellar form, penetrates minimally into normal eukaryotic HEK293T cells (Figure S4). This indicates a very high level of efficiency, with a selectivity index of approximately 10-12 (compared to non-micellar forms, which have an index of approximately 5-7). This difference is due to the combined influence of the pH sensitivity of the dye and its selective permeability of micelles in cells.

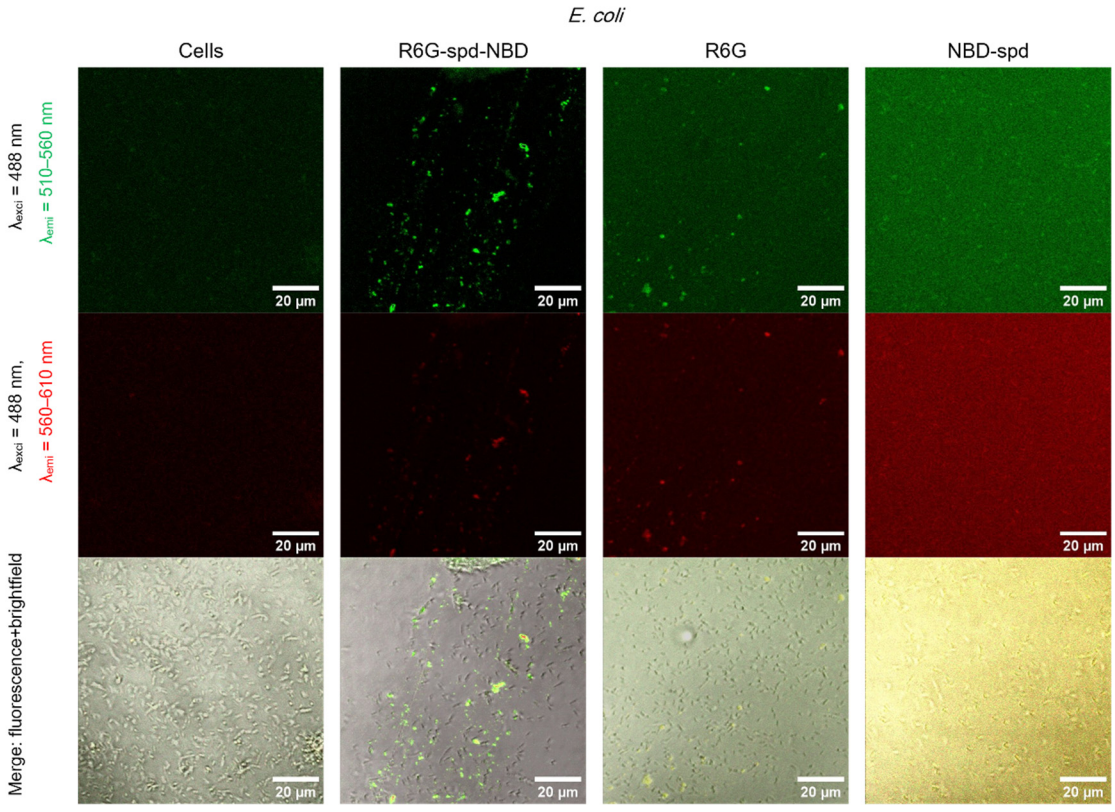

(a)

 doi:10.20944/preprints202408.0285.v1

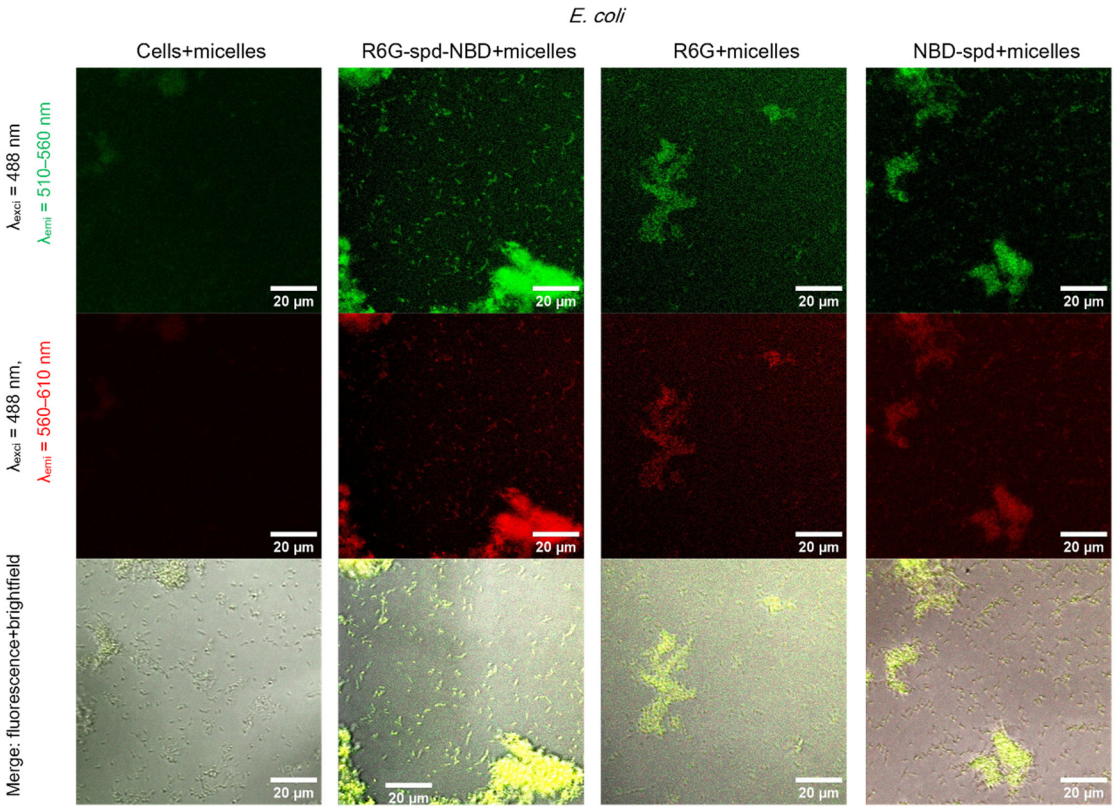

(b)

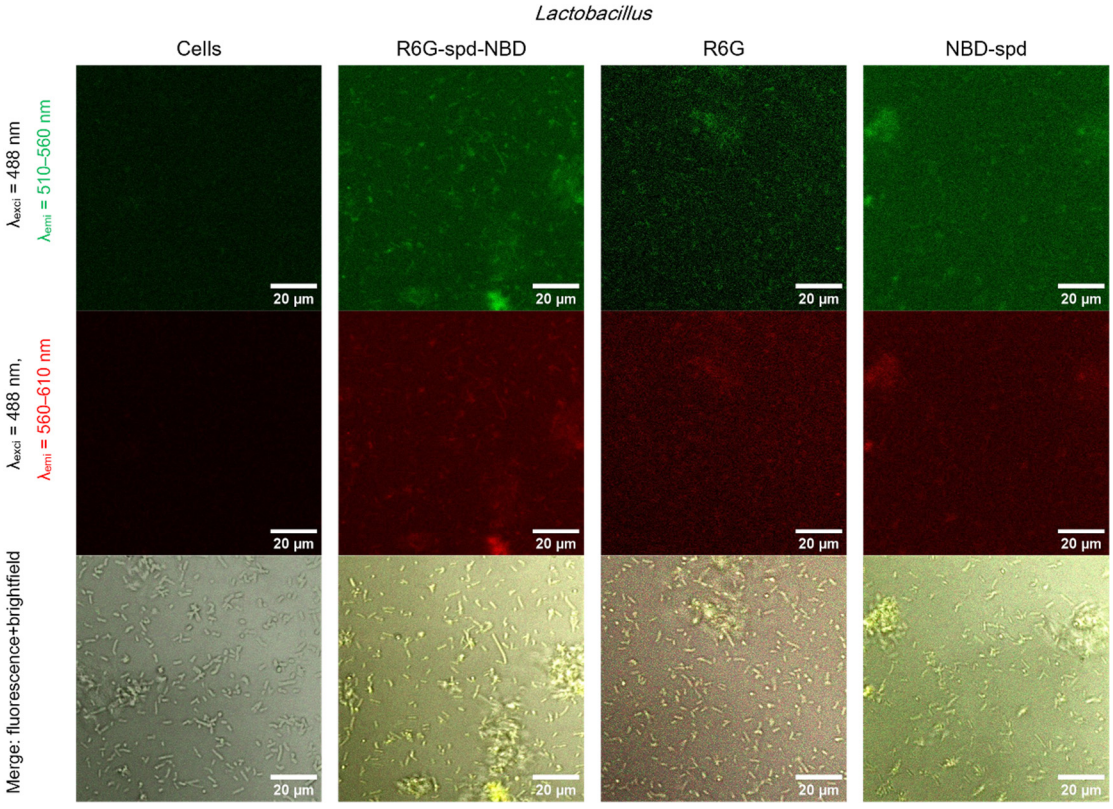

(c)

 doi:10.20944/preprints202408.0285.v1

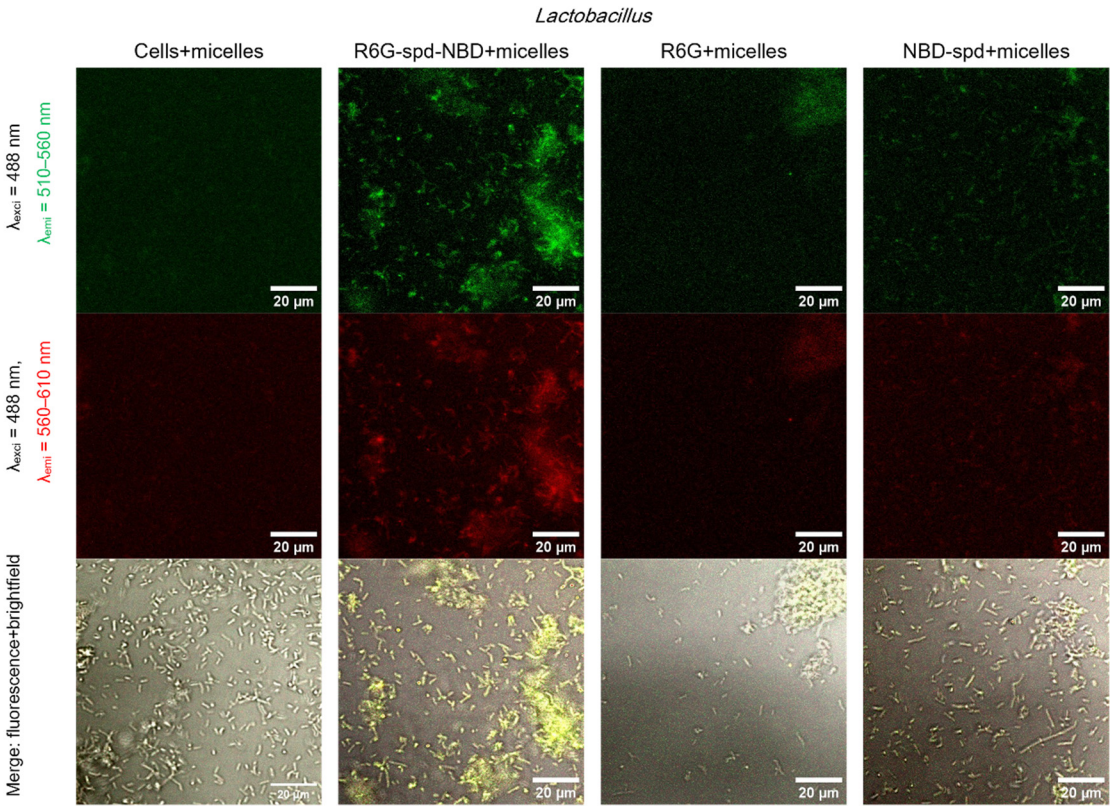

(d)

Figure 5. Confocal laser scanning microscopy images of **(a)-(b)** *E. coli* cells, **(c)-(d)** *Lactobacilli* cells, labelled with NBD-spd, R6G or R6G-spd-NBD (1 μg/mL for all markers) in free or micellar form. λ_{exci} = 488 nm, λ_{emi} = 510–560 nm (green channel), λ_{emi} = 560–610 nm (red channel). The scale bar is 20 μm. "Micelles" mean Chit5-LA polymeric micelles. C_{mic} = 0.1 mg/mL.

2.6. Fluorescence Microscopy for Visualization of Model Latent Bacterial Infections Localized in Macrophages

An important biomedical challenge is the diagnosis and treatment, or ideally both simultaneously, of latent bacterial infections that occur within macrophages. One example of a disease that requires a new approach, the use of theranostics, in relation to such a dangerous intracellular infection as brucellosis. Brucellosis is an infectious disease characterized by a variety of pathological changes in multiple organs and a propensity for chronicity.

To explore the feasibility of designing therapeutic agents capable of targeting bacterial inclusions within macrophages we have studied macrophages from human bronchoalveolar lavage (BAL) samples that have phagocytosed bacterial cells as model systems. Figure 6 illustrates fluorescence microscopy images of macrophages (large) and bacteria (small) from human BAL, labeled with either R6G-spd-NBD (Figure 6a) or R6G (1 μg/mL, all fluorophore concentrations) in a micellar form (Figure 6b). In the blue channel, macrophages' nuclei and lysosomes, which apparently contain bacteria, are visible. In the green channel, when using R6G-spd-NBD, small dots corresponding to intracellular bacteria can also be seen, in addition to macrophages' nuclei (a bright spot in the center). The ignition of micellar conjugates takes place in a mildly acidic environment, such as in lysosomes, where the pH ranges from 5.5 to 6.5. The data on the staining parameters of cellular structures within macrophages are presented in Table 2.

Rhodamine also clearly visualizes cellular structures when observed in the blue channel, although the contrast in the green channel is lower (about 3 times weaker than for the conjugate). The effect of the R6G-spd-NBD conjugate can be explained by its pH sensitivity and the enhancement of FRET during the penetration of the fluorophores into the cells. Therefore, the micellar formulation R6G-spd-NBD has the potential to be used for both the diagnosis of simple bacterial infections and

 doi:10.20944/preprints202408.0285.v1

the detection of complex, latent macrophage-associated pathogens such as brucellosis, leishmaniasis, and tuberculosis.

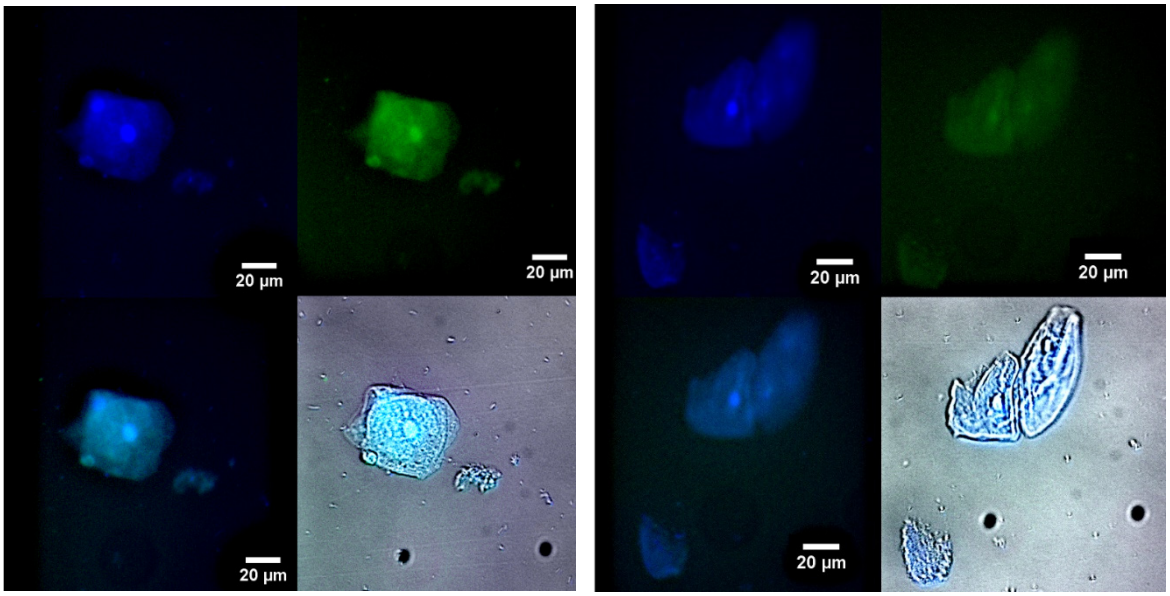

(a) **(b)**

Figure 6. Fluorescence microscopy images of macrophage (large) and bacterial (small) cells from human bronchoalveolar lavage (BAL) labelled with **(a)** R6G-spd-NBD or **(b)** R6G (1 µg/mL for all fluorophores) in micellar form. Blue channel: $\lambda_{exci,\,max}$ = 360 nm, λ_{emi} = 425–700 nm. Green channel: $\lambda_{exci,\,max}$ = 475 nm, λ_{emi} = 515–700 nm. Additionally, the blue and green overlay channels and the fluorescence overlay channel on brightfield are shown. The scale bar is 20 µm. "Micellar" mean Chit5-LA polymeric micellar formulation. C_{mic} = 0.1 mg/mL.

Table 2. Quantitative parameters of staining of cellular structures in macrophage cells: fluorescence intensity on a scale of 0-255. T = 37 °C.

Probe	Blue channel				Green channel			
	Background	Nucleus	Lysosomes	Cytoplasm	Background	Nucleus	Lysosomes	Cytoplasm
R6G-spd-NBD	14	253	250 and 134	130	2	164	105 and 108	91
R6G	22	198	130	105	16	84	62	54

We have demonstrated a remarkable increase in antibacterial activity, reaching up to 45% in terms of cellular survival. These probes exhibit a selective targeting of bacterial infections, which can be visualized, opening up opportunities for phototherapy involving the generation of reactive oxygen species.

The proposed systems represent theranostic tools, offering a groundbreaking approach to addressing challenging infectious diseases. They enhance the quality of patient care by providing a novel treatment strategy. These systems rely on the development of technologies for the targeted delivery of antibiotics specifically to macrophages containing dormant bacteria. This approach enables the combination of antibiotic treatment with fluorescence monitoring, allowing for a precise evaluation of the therapeutic process.

3. Conclusions

Theranostic approaches have the potential to revolutionize the management of chronic inflammatory conditions, associated with macrophage activity, such as leishmaniasis, brucellosis,

 doi:10.20944/preprints202408.0285.v1

and tuberculosis. The infections within macrophages, such as those caused by bacteria like *Brucella*, pose significant challenges due to their ability to persist in a latent state. We have developed a novel conjugated form of Rhodamine 6G (R6G) and 4-nitro-2,1,3-benzoxadiazole (NBD), linked by a spacer molecule, spermidine. This conjugated form, represents a promising theranostic agent with high potential which imparts the functionality of pH responsiveness and FRET function.

The micellar formulation of the R6G-spd-NBD probe exhibits remarkable sensitivity to alterations in the acidity level of the cellular milieu. The micelles formed by amphiphilic polymers with loaded probes exhibit a compact and highly spherical shape, ranging in diameter from 70 to 110 nm.

Micellar formulations R6G-spd-NBD exhibits selective staining properties towards *E. coli* and *Lactobacilli*, allowing for the visualization of macrophages containing bacteria using confocal laser scanning microscopy. Microbiological studies demonstrate an increased toxicity of the micellar form of the R6G-spd-NBD agent compared to its free form and control samples of Rhodamine 6G. Macrophages isolated from human bronchoalveolar lavage fluid (BAL) were employed to investigate the potential for developing theranostic agents providing visualizing macrophages and bacteria within BAL samples.

A micellar formulation, R6G-spd-NBD, has been demonstrated to be effective in diagnosing simple bacterial infections, as well as identifying more complex, latent pathogens. Consequently, these fluorescent probes represent promising theranostic tools that can be utilized in the detection and treatment of intricate infections involving macrophages.

4. Materials and Methods

4.1. Reagents

NBD-Cl (4-chloro-7-nitro-1,2,3-benzaxadiazole) was purchased from Thermofisher Scientific (Carlsbad, CA, USA). Rhodamine 6G (R6G), spermidine (spd), 4-hydroxybenzaldehyde, chitosan oligosaccharide lactate 5 kDa (Chit5), and lipoic acid (LA) were obtained from Sigma-Aldrich (St. Louis, MI, USA). Para-toluenesulfonic acid (TsOH), salts for the preparation of buffer solutions, NaOH, and HCl were produced by Reachim (Moscow, Russia).

4.2. Synthesis of NBD-spd-R6G Fluorophore

The synthesis of the pH-sensitive fluorophore NBD-spd-R6G was carried out in 4 stages as earlier described [59]. Briefly, in 1st stage the samples of spd and 4-hydroxybenzaldehyde were reacted with the formation of spd-N=CH-C_6H_4-OH. Then, in 2nd stage NBD-Cl was modified with spd-N=CH-C_6H_4-OH, as a result yellow-orange flakes of NBD-spd-N=CH-C_6H_4-OH were isolated. In 3rd stage 3 NBD-spd-N=CH-C_6H_4-OH was deprotected with the formation of NBD-spd product. Finally, NBD-spd was reacted with R6G. The product NBD-spd-R6G (55 mg, 0.074 mmol, yield of 76%, final yield in four stages of 46%) was isolated after freeze-drying at a temperature of –60 °C.

Spermidine (spd) NH_2 groups modification degree was determined using spectrophotometric titration (before and after modification) with 2,4,6-trinitrobenzenesulfonic acid (TNBS) in 0.02 M sodium borate buffer (pH 9.2). The number of primary titrated NH_2groups found by this method is as follows: (1) Spermidine —2 per molecule; (2) spd-N=CH-C_6H_4-OH—1 per molecule; (3) 0 NH_2– per NBD-spd-N=CH-C_6H_4-OH molecule; (4) NBD-spd—1 per molecule; (5) NBD-spd-R6G—1 per molecule.

4.3. Synthesis of Chit5-LA Amphiphilic Conjugate and Preparation of Polymeric Micellar Theranostic Formulations

The synthesis of lipoic acid (LA)-modified 5 kDa chitosan (Chit-LA) and lipoic acid (LA)-modified 12-14 kDa heparin (Hep-LA) was carried out as described by us earlier [31]. Chitosan LA-grafting degree was determined by spectrophotometric titration of amino groups using 2,4,6-trinitrobenzenesulfonic acid (by absorption at 420 nm). Chit5 was used as control sample.

 doi:10.20944/preprints202408.0285.v1

Self-assembled Chit-LA or Hep-LA polymer (2 mL, 1 mg/mL) was mixed with R6G, NBD-spd, or theranostic sensor R6G-spd-NBD (2 mL, 0.1 mg/mL) in PBS (0.01 M, pH of 7.4), and the mixtures were then incubated at 37 °C for 1 h. Micellar solutions were prepared via ultrasonic treatment of samples (22 kHz) for 10-15 min with constant cooling in an ultrasonic device (Cole-Parmer Instrument, Vernon Hills, IL, USA). Micelles samples were extruded (5-fold, 200 nm membrane, Avanti Polar Lipids). Then free fluorophores were then separated by dialysis against PBS (with a cut-off mass of 6–8 kDa), and the loading degree was determined by absorbance at 490 or 515 nm.

4.4. Characterization of Polymeric Micelles and Theranostic drugs

4.4.1. Fourier Infrared Spectroscopy

The FTIR spectra of the samples in suspension were recorded using a Bruker Tensor 27 spectrometer equipped with a liquid nitrogen-cooled MCT (cadmium–mercury telluride) detector. A total of 35 μL of samples was placed in a thermostatically controlled (22 or 37 °C) BioATR-II cell with a ZnSe element (Bruker, Bremen, Germany), and IR spectra in the range from 850 to 4000 cm^{-1} with a spectral resolution of 1 cm^{-1} were recorded. A total of 70 scans were accumulated and averaged for each spectrum. Spectral data were processed using the Bruker Opus 8.2.28 program (Bruker, Bremen, Germany).

4.4.2. NMR Spectroscopy

^{1}H NMR and ^{13}C NMR spectra were recorded on a Bruker DRX-500 instrument [working frequencies of 500.13 MHz (^{1}H) and 125.76 MHz (^{13}C)]. Chemical shifts were given in parts per million (ppm) and assigned to the appropriate NMR solvent peaks.

4.4.3. Fluorescence Spectroscopy

Fluorescence emission and excitation were measured using a Varian Cary Eclipse fluorescence spectrophotometer (Agilent Technologies, Santa Clara, CA, USA) at temperatures of 22 and 37 °C. $\lambda_{excitation}$ = 460 or 515 nm. $\lambda_{emission}$ = 550 nm.

4.4.4. Circular Dichroism Spectroscopy

Circular dichroism (CD) spectra were recorded on Jasco J-815 CD Spectrometer (JASCO, Tokyo, Japan) and were used to calculate the chitosan deacetylation degree, which amounted to (95 ± 2%).

4.4.5. Atomic Force Microscopy

Atomic force microscopy (AFM microscope NTEGRA II, NT-MDT Spectrum Instruments, Moscow, Russia) was used to study polymeric micelles' topology and size.

4.4.6. Dynamic Light Scattering

Dynamic Light Scattering (DLS) was used to measure the particle sizes and zeta potentials using a Zetasizer Nano S "Malvern" (Worcestershire, UK).

4.5. Microbiology Experiments

4.5.1. Bacterial Cells Cultivation

The strains used in this study were *Escherichia coli* (ATCC 25922) from the National Resource Center Russian collection of industrial microor- ganisms, SIC "Kurchatov Institute" and *Lactobacillus* (commercially available pharmaceutical Lactobacillus Liquid Concentrate). The cultures were cultivated for 18–20 h at 37 °C to a CFU/mL ≈ 2×10^{7} (determined by measuring A_{600} and by seeding on petri dishes) in the liquid nutrient medium Luria–Bertani (pH 7.2) with stirring 120 rpm.

 doi:10.20944/preprints202408.0285.v1

4.5.2. Antibacterial Studies

The cell suspensions (10^7 CFU/mL) were incubated with the R6G, NBD-spd or R6G-spd-NBD-containing samples (free and micellar form). The specimens were incubated at 37 °C for 24 h. After incubation, the number of surviving cells was determined by A700 and controlled by quantitative seeding on Petri dishes. The dishes were placed in the incubator at 37 °C for 24 h. Then, the number of colonies (CFU) was counted.

4.5.3. Visualization of Petri Dishes with Bacteria Incubated with Fluorophores

Fluorescent image of a Petri dish with *E. coli* cells (10^7 CFU / 0.5 mL placed onto 20 mL of agarized medium) when exposed to R6G or R6G-spd-NBD in non-micellar and micellar form for 12 h at 37 °C were obtained with a UVP BioSpectrum imaging system (BioSpectrum; UVP, Upland, CA, USA). The fluorophores are placed in wells with a diameter of 9 mm. The concentration of fluorophores is 0.1 mg/mL, the concentration of amphiphilic polymers is 0.5 mg/mL. $\lambda_{exci,\,max}$ = 480 nm. λ_{emi} = 515-570 nm.

4.6. Confocal Laser Scanning Microscopy (CLSM) and Fluorescence microscopy

4.6.1. CLSM Visualization of Bacterial Cell Staining Using a Theranostic Preparation

Bacterial cells (5 × 10^6 cells/mL) were incubated with 1 μM of NBD-spd, R6G, or R6G-spd-NBD in a free or micellar (0.1 mg/mL Chit-LA or Hep-LA) form, followed by double washing (5 min, 8000×g) and transfer to the wells of a 96-well plate. The cells were then imaged using a CLSM. The cells are fixed with a paraform and filled with 70 μl of 50% glycerin-PBS/

CLSM images were obtained using the confocal laser scanning microscope Olympus FluoView FV1000 equipped with both a spectral version scan unit with emission detectors and a transmitted light detector. CLSM is based on the motorized inverted microscope Olympus IX81. The excitation wavelength 488 nm (multiline Argon laser) and dry objective lens Olympus UPLSAPO 40X NA 0.90 were used for the measurements. Laser power, sampling speed, and averaging were the same for all image acquisitions. The scan area was 80 × 80 μm². Fluorescence was collected using the emission windows set at 510–560 nm (green channel) and 560–610 nm (red channel). The signals were adjusted to the linear range of the detectors. Olympus FV10 ASW 1.7 software was used for acquisition of the images.

4.6.2. Fluorescence Microscopy for Visualization of Model Latent Bacterial Infections Localized in Macrophages

Macrophages with CD206 expression, both with and without absorbed bacteria, were captured on a polymer chip coated with mannan [44,64]. The macrophages were then incubated with theranostics agents for 3 hours. Following this, the macrophages were washed to remove any free fluorophores and transferred to the wells of 8-well plate, where it was fixed with paraformaldehyde and analyzed using fluorescence microscopy.

Fluorescence images were obtained using a IX81 motorized inverted microscope (Olympus, Tokyo, Japan). A short-arc xenon lamp with a power of 75 W was used as a light source for the fluorescence excitation, and a halogen lamp was used as a light source for transmitted light imaging. Images were acquired using the UPlanSApo 20× NA 0.75 objective lens and U-MWU2 fluorescent filter cube and recorded using the XM10-cooled CCD monochrome camera (all from Olympus, Tokyo, Japan). Cell Sens imaging software (v.3.2, Olympus, Tokyo, Japan) was used for microscope and camera control. The use of a fluorescence microscope instead of a confocal laser scanning microscope was due to the fact that ultraviolet light was required to excite fluorescence. Blue channel: $\lambda_{exci,\,max}$ = 360 nm, λ_{emi} = 425–700 nm. Green channel: $\lambda_{exci,\,max}$ = 475 nm, λ_{emi} = 515–700 nm. Additionally, the blue and green overlay channels and the fluorescence overlay channel on brightfield are shown. The scale bar is 20 μm.

Supplementary Materials: The following supporting information can be downloaded at the website of this paper posted on Preprints.org. **Figure S1.** Synthesis scheme of the pH-sensitive fluorophore NBD-spd-R6G. The products are a mixture of isomers (because spermidine is not symmetrical). **Figure S2.** FTIR spectra of initial compounds, intermediate substances, and product of synthesis of pH-sensitive fluorophore R6G-spd-NBD: (**a**) stage 1, (**b**) stage 2, (**c**) stage 3, (**d**) stage 4. Aqueous solutions. T = 22 °C. **Figure S3.** ^{1}H NMR spectra of NBD-spd. T = 22 °C. DMSO-d_6, 500 MHz.

Author Contributions: Conceptualization, E.V.K. and I.D.Z.; methodology, I.D.Z., N.G.B., A.A.E., E.V.K.; formal analysis, I.D.Z. and A.A.E.; investigation, I.D.Z., A.A.E., N.G.B., and E.V.K.; data curation, I.D.Z. and A.A.E.; writing—original draft preparation, I.D.Z.; writing—review and editing, E.V.K.; project supervision, E.V.K.; funding acquisition, E.V.K. All authors have read and agreed to the published version of the manuscript.

Funding: This research was funded by the Russian Science Foundation, grant number 24-25-00104.

Institutional Review Board Statement: Cell lines were obtained from Lomonosov Moscow State University Depository of Live Systems Collection (Moscow, Russia).

Informed Consent Statement: Not applicable

Data Availability Statement: The data presented in this study are available in the main text and in Supplement.

Acknowledgments: This work was performed using the following equipment from the program for the development of Moscow State University: FTIR microscope MICRAN-3, Jasco J-815 CD Spectrometer, and AFM microscope NTEGRA II.

Conflicts of Interest: The authors declare no conflicts of interest.

References

1. Yordanova, A.; Eppard, E.; Kürpig, S.; Bundschuh, R.A.; Schönberger, S.; Gonzalez-Carmona, M.; Feldmann, G.; Ahmadzadehfar, H.; Essler, M. Theranostics in Nuclear Medicine Practice. *Onco. Targets. Ther.* **2017**, *10*, 4821–4828, doi:10.2147/OTT.S140671.
2. Feng, G.; Liu, B. Multifunctional AIEgens for Future Theranostics. *Small* **2016**, *12*, 6528–6535, doi:10.1002/smll.201601637.
3. Pusuluri, A.; Krishnan, V.; Wu, D.; Shields, C.W.; Wang, L.W.; Mitragotri, S. Role of Synergy and Immunostimulation in Design of Chemotherapy Combinations: An Analysis of Doxorubicin and Camptothecin. *Bioeng. Transl. Med.* **2019**, *4*, 1–11, doi:10.1002/btm2.10129.
4. Chen, X.; Wong, S.T.C. Cancer Theranostics: An Introduction. *Cancer Theranostics* **2014**, 3–8, doi:10.1016/B978-0-12-407722-5.00001-3.
5. Kelkar, S.S.; Reineke, T.M. Theranostics: Combining Imaging and Therapy. *Bioconjug. Chem.* **2011**, *22*, 1879–1903, doi:10.1021/bc200151q.
6. Weber, W.A.; Barthel, H.; Bengel, F.; Eiber, M.; Herrmann, K.; Schäfers, M. What Is Theranostics? *J. Nucl. Med.* **2023**, *64*, 669–670, doi:10.2967/jnumed.123.265670.
7. Kalash, R.S.; Lakshmanan, V.K.; Cho, C.S.; Park, I.K. Theranostics. *Biomater. Nanoarchitectonics* **2016**, 197–215, doi:10.1016/B978-0-323-37127-8.00012-1.
8. Dalhoff, A. Global Fluoroquinolone Resistance Epidemiology and Implictions for Clinical Use. *Interdiscip. Perspect. Infect. Dis.* **2012**, *2012*, doi:10.1155/2012/976273.
9. Kalelkar, P.P.; Riddick, M.; García, A.J. Biomaterial-Based Antimicrobial Therapies for the Treatment of Bacterial Infections. *Nat. Rev. Mater.* **2022**, *7*, 39–54, doi:10.1038/s41578-021-00362-4.
10. Sharma, R.; O'Sullivan, K.M.; Holdsworth, S.R.; Bardin, P.G.; King, P.T. Visualizing Macrophage Extracellular Traps Using Confocal Microscopy. *J. Vis. Exp.* **2017**, *2017*, 1–8, doi:10.3791/56459.
11. Bhat, A.R.; Wani, F.A.; Behera, K.; Khan, A.B.; Patel, R. Formulation of Biocompatible Microemulsions for Encapsulation of Anti-TB Drug Rifampicin: A Physicochemical and Spectroscopic Study. *Colloids Surfaces A Physicochem. Eng. Asp.* **2022**, *645*, 128846, doi:10.1016/j.colsurfa.2022.128846.
12. Chen, X.; Zhou, Q.; Tan, Y.; Wang, R.; Wu, X.; Liu, J.; Liu, R.; Wang, S.; Dong, S. Nanoparticle-Based Lateral Flow Biosensor Integrated With Loop-Mediated Isothermal Amplification for Rapid and Visual Identification of Chlamydia Trachomatis for Point-of-Care Use. *Front. Microbiol.* **2022**, *13*, 1–13, doi:10.3389/fmicb.2022.914620.
13. Alshamrani, M. Broad-Spectrum Theranostics and Biomedical Application of Functionalized Nanomaterials. *Polymers (Basel).* **2022**, *14*, 1221, doi:10.3390/polym14061221.

14. Qi, X.; Grafskaia, E.; Yu, Z.; Shen, N.; Fedina, E.; Masyutin, A.; Erokhina, M.; Lepoitevin, M.; Lazarev, V.; Zigangirova, N.; et al. Methylene Blue-Loaded NanoMOFs: Accumulation in Chlamydia Trachomatis Inclusions and Light/Dark Antibacterial Effects. *ACS Infect. Dis.* **2023**, *9*, 1558–1569, doi:10.1021/acsinfecdis.3c00131.
15. Rai, M.; Jamil, B. *Nanotheranostics: Applications and Limitations*; 2019; ISBN 9783030297688.
16. Bai, D.P.; Lin, X.Y.; Huang, Y.F.; Zhang, X.F. Theranostics Aspects of Various Nanoparticles in Veterinary Medicine. *Int. J. Mol. Sci.* **2018**, *19*, doi:10.3390/ijms19113299.
17. Hernández-Giottonini, K.Y.; Arellano-Reynoso, B.; Rodríguez-Córdova, R.J.; de la Vega-Olivas, J.; Díaz-Aparicio, E.; Lucero-Acuña, A. Enhancing Therapeutic Efficacy against Brucella Canis Infection in a Murine Model Using Rifampicin-Loaded PLGA Nanoparticles. *ACS Omega* **2023**, *8*, 49362–49371, doi:10.1021/acsomega.3c07892.
18. Arshad, R.; Sargazi, S.; Fatima, I.; Mobashar, A.; Rahdar, A.; Ajalli, N.; Kyzas, G.Z. Nanotechnology for Therapy of Zoonotic Diseases: A Comprehensive Overview. *ChemistrySelect* **2022**, *7*, doi:10.1002/slct.202201271.
19. Prasad, M.; Ghosh, M.; Kumar, R.; Brar, B.; Surjith, K.P.; Lambe, U.P.; Ranjan, K.; Banerjee, S.; Prasad, G.; Kumar Khurana, S.; et al. The Importance of Nanomedicine in Prophylactic and Theranostic Intervention of Bacterial Zoonoses and Reverse Zoonoses in the Era of Microbial Resistance. *J. Nanosci. Nanotechnol.* **2021**, *21*, 3404–3452, doi:10.1166/jnn.2021.18999.
20. Chaubey, P.; Mishra, B.; Mudavath, S.L.; Patel, R.R.; Chaurasia, S.; Sundar, S.; Suvarna, V.; Monteiro, M. Mannose-Conjugated Curcumin-Chitosan Nanoparticles: Efficacy and Toxicity Assessments against Leishmania Donovani. *Int. J. Biol. Macromol.* **2018**, *111*, 109–120, doi:10.1016/j.ijbiomac.2017.12.143.
21. Nahar, M.; Dubey, V.; Mishra, D.; Mishra, P.K.; Dube, A.; Jain, N.K. In Vitro Evaluation of Surface Functionalized Gelatin Nanoparticles for Macrophage Targeting in the Therapy of Visceral Leishmaniasis . *J. Drug Target.* **2009**, *00*, 090729062238077–13, doi:10.1080/10611860903115290.
22. Kunjachan, S.; Gupta, S.; Dwivedi, A.K.; Dube, A.; Chourasia, M.K. Chitosan-Based Macrophage-Mediated Drug Targeting for the Treatment of Experimental Visceral Leishmaniasis. *J. Microencapsul.* **2011**, *28*, 301–310, doi:10.3109/02652048.2011.559281.
23. Shadman, M. Diagnosis and Treatment of Chronic Lymphocytic Leukemia: A Review. *Jama* **2023**, *329*, 918–932, doi:10.1001/jama.2023.1946.
24. Huynh, N.T.; Roger, E.; Lautram, N.; Benoît, J.P.; Passirani, C. The Rise and Rise of Stealth Nanocarriers for Cancer Therapy: Passive versus Active Targeting. *Nanomedicine* **2010**, *5*, 1415–1433, doi:10.2217/nnm.10.113.
25. Zhang, M.; Asghar, S.; Jin, X.; Hu, Z.; Ping, Q.; Chen, Z.; Shao, F.; Xiao, Y. The Enhancing Effect of N-Acetylcysteine Modified Hyaluronic Acid-Octadecylamine Micelles on the Oral Absorption of Paclitaxel. *Int. J. Biol. Macromol.* **2019**, *138*, 636–647, doi:10.1016/j.ijbiomac.2019.07.114.
26. Xu, W.; Wang, H.; Dong, L.; Zhang, P.; Mu, Y.; Cui, X.; Zhou, J.; Huo, M.; Yin, T. Hyaluronic Acid-Decorated Redox-Sensitive Chitosan Micelles for Tumor-Specific Intracellular Delivery of Gambogic Acid. *Int. J. Nanomedicine* **2019**, *14*, 4649–4666, doi:10.2147/IJN.S201110.
27. Zari, A.T.; Zari, T.A.; Hakeem, K.R. Anticancer Properties of Eugenol : A Review. **2021**.
28. Kashyap, B.K.; Singh, V.V.; Solanki, M.K.; Kumar, A.; Ruokolainen, J.; Kesari, K.K. Smart Nanomaterials in Cancer Theranostics: Challenges and Opportunities. *ACS Omega* **2023**, *8*, 14290–14320, doi:10.1021/acsomega.2c07840.
29. Bhushan, A.; Gonsalves, A.; Menon, J.U. Current State of Breast Cancer Diagnosis, Treatment, and Theranostics. *Pharmaceutics* **2021**, *13*, 1–24, doi:10.3390/pharmaceutics13050723.
30. Arranja, A.G.; Pathak, V.; Lammers, T.; Shi, Y. Tumor-Targeted Nanomedicines for Cancer Theranostics. *Pharmacol. Res.* **2017**, *115*, 87–95, doi:10.1016/j.phrs.2016.11.014.
31. Zlotnikov, I.D.; Ezhov, A.A.; Dobryakova, N. V.; Kudryashova, E. V. Disulfide Cross-Linked Polymeric Redox-Responsive Nanocarrier Based on Heparin, Chitosan and Lipoic Acid Improved Drug Accumulation, Increased Cytotoxicity and Selectivity to Leukemia Cells by Tumor Targeting via "Aikido" Principle. *Gels* **2024**, *10*, 157, doi:10.3390/gels10030157.
32. Radeva, L.; Yordanov, Y.; Spassova, I.; Kovacheva, D.; Tzankova, V.; Yoncheva, K. Double-Loaded Doxorubicin/Resveratrol Polymeric Micelles Providing Low Toxicity on Cardiac Cells and Enhanced Cytotoxicity on Lymphoma Cells. *Pharmaceutics* **2023**, *15*, doi:10.3390/pharmaceutics15041287.
33. Cho, K.; Wang, X.; Nie, S.; Chen, Z.; Shin, D.M. Therapeutic Nanoparticles for Drug Delivery in Cancer. *Clin. Cancer Res.* **2008**, *14*, 1310–1316, doi:10.1158/1078-0432.CCR-07-1441.

34. Zlotnikov, I.D.; Streltsov, D.A.; Ezhov, A.A.; Kudryashova, E. V. Smart PH- and Temperature-Sensitive Micelles Based on Chitosan Grafted with Fatty Acids to Increase the Efficiency and Selectivity of Doxorubicin and Its Adjuvant Regarding the Tumor Cells. *Pharmaceutics* **2023**, *15*, 1135, doi:10.3390/pharmaceutics15041135.
35. Zlotnikov, I.D.; Kudryashova, E. V Smart Polymeric Micelles System , Designed to Carry a Combined Cargo of L-Asparaginase and Doxorubicin , Shows Vast Improve- Ment in Cytostatic Efficacy. **2024**, *4*, 1–26.
36. Zlotnikov, I.D.; Belogurova, N.G.; Krylov, S.S.; Semenova, M.N.; Semenov, V. V.; Kudryashova, E. V. Plant Alkylbenzenes and Terpenoids in the Form of Cyclodextrin Inclusion Complexes as Antibacterial Agents and Levofloxacin Synergists. *Pharmaceuticals* **2022**, *15*, doi:10.3390/ph15070861.
37. Zlotnikov, I.D.; Dobryakova, N. V.; Ezhov, A.A.; Kudryashova, E. V. Achievement of the Selectivity of Cytotoxic Agents against Cancer Cells by Creation of Combined Formulation with Terpenoid Adjuvants as Prospects to Overcome Multidrug Resistance. *Int. J. Mol. Sci.* **2023**, *24*, 8023, doi:10.3390/ijms24098023.
38. Nandakumar, V.; Hebrink, D.; Jenson, P.; Kottom, T.; Limper, A.H. Differential Macrophage Polarization from Pneumocystis in Immunocompetent and Immunosuppressed Hosts: Potential Adjunctive Therapy during Pneumonia. *Infect. Immun.* **2017**, *85*, doi:10.1128/IAI.00939-16.
39. Ying, W.; Cheruku, P.S.; Bazer, F.W.; Safe, S.H.; Zhou, B. Investigation of Macrophage Polarization Using Bone Marrow Derived Macrophages. *J. Vis. Exp.* **2013**, 1–8, doi:10.3791/50323.
40. Draijer, C.; Robbe, P.; Boorsma, C.E.; Hylkema, M.N.; Melgert, B.N. Characterization of Macrophage Phenotypes in Three Murine Models of House-Dust-Mite-Induced Asthma. *Mediators Inflamm.* **2013**, *2013*, 1–11, doi:10.1155/2013/632049.
41. Maev, I. V.; Lyamina, S. V.; Malysheva, E. V.; Yurenev, G.L.; Malyshev, I.Y. An Immune Response and an Alveolar Macrophage Phenotype in Asthma, Gastroesophageal Reflux Disease and Their Concurrence. *Ter. Arkh.* **2015**, *87*, 34–41, doi:10.17116/terarkh201587334-41.
42. Brundu S, F.A. Polarization and Repolarization of Macrophages. *J. Clin. Cell. Immunol.* **2015**, *06*, doi:10.4172/2155-9899.1000319.
43. Porta, C.; Riboldi, E.; Totaro, M.G.; Strauss, L.; Sica, A.; Mantovani, A. Macrophages in Cancer and Infectious Diseases: The 'good' and the 'Bad'. *Immunotherapy* **2011**, *3*, 1185–1202, doi:10.2217/imt.11.116.
44. Savchenko, I. V.; Zlotnikov, I.D.; Kudryashova, E. V. Biomimetic Systems Involving Macrophages and Their Potential for Targeted Drug Delivery. *Biomimetics* **2023**, *8*, doi:10.3390/biomimetics8070543.
45. Hong, J.Y.; Chung, Y.; Steenrod, J.; Chen, Q.; Lei, J.; Comstock, A.T.; Goldsmith, A.M.; Bentley, J.K.; Sajjan, U.S.; Hershenson, M.B. Macrophage Activation State Determines the Response to Rhinovirus Infection in a Mouse Model of Allergic Asthma. *Respir. Res.* **2014**, *15*, 1–15, doi:10.1186/1465-9921-15-63.
46. Staples, K.J.; Hinks, T.S.C.; Ward, J.A.; Gunn, V.; Smith, C.; Djukanović, R. Phenotypic Characterization of Lung Macrophages in Asthmatic Patients: Overexpression of CCL17. *J. Allergy Clin. Immunol.* **2012**, *130*, 1404-1412.e7, doi:10.1016/j.jaci.2012.07.023.
47. Ruan, G.X.; Chen, Y.Z.; Yao, X.L.; Du, A.; Tang, G.P.; Shen, Y.Q.; Tabata, Y.; Gao, J.Q. Macrophage Mannose Receptor-Specific Gene Delivery Vehicle for Macrophage Engineering. *Acta Biomater.* **2014**, *10*, 1847–1855, doi:10.1016/j.actbio.2014.01.012.
48. Di Benedetto, P.; Ruscitti, P.; Vadasz, Z.; Toubi, E.; Giacomelli, R. Macrophages with Regulatory Functions, a Possible New Therapeutic Perspective in Autoimmune Diseases. *Autoimmun. Rev.* **2019**, *18*, 102369, doi:10.1016/j.autrev.2019.102369.
49. Sharma, N.; Akkoyunlu, M.; Rabin, R.L. Macrophages—Common Culprit in Obesity and Asthma. *Allergy Eur. J. Allergy Clin. Immunol.* **2018**, *73*, 1196–1205, doi:10.1111/all.13369.
50. Kelly, C.; Jefferies, C.; Cryan, S.-A. Targeted Liposomal Drug Delivery to Monocytes and Macrophages. *J. Drug Deliv.* **2011**, *2011*, 1–11, doi:10.1155/2011/727241.
51. Peyron, P.; Vaubourgeix, J.; Poquet, Y.; Levillain, F.; Botanch, C.; Bardou, F.; Daffé, M.; Emile, J.F.; Marchou, B.; Cardona, P.J.; et al. Foamy Macrophages from Tuberculous Patients' Granulomas Constitute a Nutrient-Rich Reservoir for M. Tuberculosis Persistence. *PLoS Pathog.* **2008**, *4*, 1–14, doi:10.1371/journal.ppat.1000204.
52. Dua, K.; Rapalli, V.K.; Shukla, S.D.; Singhvi, G.; Shastri, M.D.; Chellappan, D.K.; Satija, S.; Mehta, M.; Gulati, M.; Pinto, T.D.J.A.; et al. Multi-Drug Resistant Mycobacterium Tuberculosis & Oxidative Stress Complexity: Emerging Need for Novel Drug Delivery Approaches. *Biomed. Pharmacother.* **2018**, *107*, 1218–1229, doi:10.1016/j.biopha.2018.08.101.

53. Laval, T.; Chaumont, L.; Demangel, C. Not Too Fat to Fight: The Emerging Role of Macrophage Fatty Acid Metabolism in Immunity to Mycobacterium Tuberculosis. *Immunol. Rev.* **2021**, *301*, 84–97, doi:10.1111/imr.12952.
54. Tulu, D. Bovine Brucellosis: Epidemiology, Public Health Implications, and Status of Brucellosis in Ethiopia. *Vet. Med. Res. Reports* **2022**, *Volume 13*, 21–30, doi:10.2147/VMRR.S347337.
55. Di Bonaventura, G.; Angeletti, S.; Ianni, A.; Petitti, T.; Gherardi, G. Microbiological Laboratory Diagnosis of Human Brucellosis: An Overview. *Pathogens* **2021**, *10*, 1623, doi:10.3390/pathogens10121623.
56. Khurana, S.K.; Sehrawat, A.; Tiwari, R.; Prasad, M.; Gulati, B.; Shabbir, M.Z.; Chhabra, R.; Karthik, K.; Patel, S.K.; Pathak, M.; et al. Bovine Brucellosis – a Comprehensive Review. *Vet. Q.* **2021**, *41*, 61–88, doi:10.1080/01652176.2020.1868616.
57. Boon, T.H.; Williams, E. DIAGNOSIS OF BRUCELLOSIS. *Lancet* **1970**, *296*, 51, doi:10.1016/S0140-6736(70)92522-5.
58. Corbel, M. Brucellosis: An Overview. *Emerg. Infect. Dis.* **1997**, *3*, 213–221, doi:10.3201/eid0302.970219.
59. Zlotnikov, I.D.; Ezhov, A.A.; Kudryashova, E. V. PH-Sensitive Fluorescent Marker Based on Rhodamine 6G Conjugate with Its FRET/PeT Pair in "Smart" Polymeric Micelles for Selective Imaging of Cancer Cells. *Pharmaceutics* **2024**, *16*, 1007, doi:10.3390/pharmaceutics16081007.
60. Huster, D.; Müller, P.; Arnold, K.; Herrmann, A. Dynamics of Membrane Penetration of the Fluorescent 7-Nitrobenz-2-Oxa-1,3-Diazol-4-Yl (NBD) Group Attached to an Acyl Chain of Phosphatidylcholine. *Biophys. J.* **2001**, *80*, 822–831, doi:10.1016/S0006-3495(01)76061-4.
61. Cao, X.J.; Chen, L.N.; Zhang, X.; Liu, J.T.; Chen, M.Y.; Wu, Q.R.; Miao, J.Y.; Zhao, B.X. A NBD-Based Simple but Effective Fluorescent PH Probe for Imaging of Lysosomes in Living Cells. *Anal. Chim. Acta* **2016**, *920*, 86–93, doi:10.1016/j.aca.2016.03.029.
62. Kraithong, S.; Sangsuwan, R.; Worawannotai, N.; Sirirak, J.; Charoenpanich, A.; Thamyongkit, P.; Wanichachewa, N. Triple Detection Modes for Hg2+ Sensing Based on a NBD-Fluorescent and Colorimetric Sensor and Its Potential in Cell Imaging. *New J. Chem.* **2018**, *42*, 12412–12420, doi:10.1039/c8nj01915k.
63. Song, F.; Li, Z.; Li, J.; Wu, S.; Qiu, X.; Xi, Z.; Yi, L. Investigation of Thiolysis of NBD Amines for the Development of H2S Probes and Evaluating the Stability of NBD Dyes. *Org. Biomol. Chem.* **2016**, *14*, 11117–11124, doi:10.1039/c6ob02354a.
64. Zlotnikov, I.D.; Kudryashova, E. V. Biomimetic System Based on Reconstituted Macrophage Membranes for Analyzing and Selection of Higher-Affinity Ligands Specific to Mannose Receptor to Develop the Macrophage-Focused Medicines. *Biomedicines* **2023**, *11*, doi:10.3390/biomedicines11102769.